Geometric Calibration of Lens and Filter Distortions for Multispectral Filter Wheel Cameras

Johannes Brauers and Til Aach
Institute of Imaging and Computer Vision
RWTH Aachen University, 52056 Aachen, Germany
tel: +49 241 80 27860, fax: +49 241 80 22200
web: www.lfb.rwth-aachen.de

in: IEEE Transactions on Image Processing. See also BibTeX entry below.

BibTeX:

```
@article{BRA11a,
author = {Johannes Brauers and Til Aach},
title = {Geometric Calibration of Lens and Filter Distortions for Multispectral
                            Filter Wheel Cameras},
journal = {IEEE Transactions on Image Processing},
volume = {20},
number = {2},
year = {2011},
pages = {496--505}}
```

Geometric Calibration of Lens and Filter Distortions for Multispectral Filter-Wheel Cameras

Johannes Brauers and Til Aach, *Senior Member, IEEE*

***Abstract*—High-fidelity color image acquisition with a multispectral camera utilizes optical filters to separate the visible electromagnetic spectrum into several passbands. This is often realized with a computer-controlled filter wheel, where each position is equipped with an optical bandpass filter. For each filter wheel position, a grayscale image is acquired and the passbands are finally combined to a multispectral image. However, the different optical properties and non-coplanar alignment of the filters cause image aberrations since the optical path is slightly different for each filter wheel position. As in a normal camera system, the lens causes additional wavelength-dependent image distortions called chromatic aberrations. When transforming the multispectral image with these aberrations into an RGB image, color fringes appear, and the image exhibits a pincushion or barrel distortion. In this paper, we address both the distortions caused by the lens and by the filters. Based on a physical model of the bandpass filters, we show that the aberrations caused by the filters can be modeled by displaced image planes. The lens distortions are modeled by an extended pinhole camera model, which results in a remaining mean calibration error of only 0.07 pixels. Using an absolute calibration target, we then geometrically calibrate each passband and compensate for both lens and filter distortions simultaneously. We show that both types of aberrations can be compensated and present detailed results on the remaining calibration errors.**

***Index Terms*—Camera calibration, chromatic aberration, geometric distortion, multispectral image processing, multispectral imaging model.**

I. Introduction

FAITHFUL color reproduction required in the textile industry [1], printing industry [2], archiving of paintings [3] and many other applications depends upon the quality of color image acquisition. Conventional RGB cameras exhibit a systematic color error because their spectral sensitivity curves are not a linear combination of the CIE observer and, thus, violate the Luther rule [4]. Multispectral cameras, on the other hand, separate the visible electromagnetic spectrum into more than six passbands, and they allow an improved reproduction of colors [5], [6].

Manuscript received August 25, 2009; revised June 01, 2010; accepted July 21, 2010. Date of publication July 29, 2010; date of current version January 14, 2011. This work was supported by the German Research Foundation (DFG, Grant AA5/2-1). The associate editor coordinating the review of this manuscript and approving it for publication was Dr. Xiaolin Wu.

The authors are with the Institute of Imaging and Computer Vision, RWTH Aachen University, D-52056 Aachen, Germany (e-mail: Johannes.Brauers@lfb.rwth-aachen.de; Til.Aach@lfb.rwth-aachen.de).

Color versions of one or more of the figures in this paper are available online at http://ieeexplore.ieee.org.

Digital Object Identifier 10.1109/TIP.2010.2062193

Fig. 1. Picture of our multispectral camera. Its internal assembly is shown in Fig. 2.

Several approaches to perform multispectral imaging are introduced in the literature. A spectral line camera using a grating to split the spectrum into its components by diffraction is described in [7]. A liquid-crystal tunable filter (LCTF), whose bandpass characteristic can be controlled by the applied voltage, can be found in [8]. Using additional, specialized filters, an RGB camera can also be converted into a multispectral camera [9], [10]. Another, well-established multispectral camera type utilizes a computer-controlled filter wheel with optical bandpass filters [11]. Several research groups [6], [12]–[15] use this kind of camera.

We use a multispectral imaging system with bandpass filters, where the filter wheel is placed between the sensor and the lens (see Fig. 2). This kind of camera exhibits three main advantages compared to a system where the filter wheel is placed between the lens and the object. First, smaller and cheaper filters can be selected and the overall size and costs of the system are, therefore, reduced. Second, the lens rather than the filter wheel is the only optical element outside the casing, and all damageable movable parts are inside the camera. Third, in our configuration, the lens can be easily exchanged like in a consumer single lens reflex camera system. For instance, a long telephoto lens could be easily exchanged by a wide angle lens without changing the camera setup.

However, placing the bandpass filters in a critical section of the optical path, namely between lens and sensor, has its downsides. When a bandpass filter is brought into the optical path of a system, which has been designed without the additional filter, the resulting image is blurred and displaced with respect to the image acquired without filter. While this problem can be partially dealt with by adjusting the focus and just accepting the displacement, multiple filters cause another problem. The different optical properties of the bandpass filters like thickness, refraction index and their pose in the filter wheel cause different

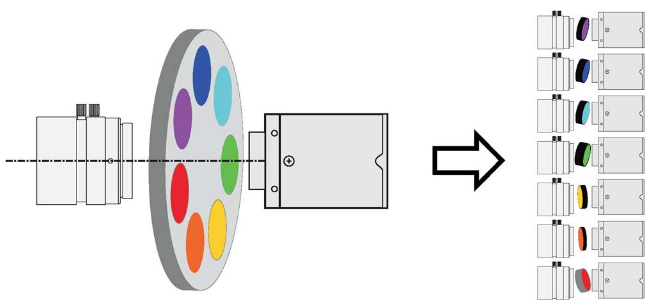

Fig. 2. A sketch of our multispectral filter wheel camera is shown on the left. In this paper, we regard the spectral channels as separate camera systems with different optical bandpass filters.

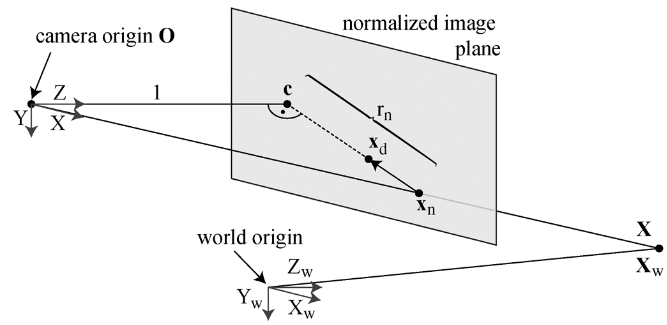

Fig. 3. Camera calibration model. An object point $\mathbf{X}$ is projected onto the point $\mathbf{x}_n$ in the normalized image plane, situated at $Z = 1$ on the Z-axis (or optical axis). Lens distortions cause the point to be shifted towards the image center $\mathbf{c}$ to $\mathbf{x}_d$. With respect to the world coordinate system, the object point is at $\mathbf{X}_w$.

aberrations. Since it is unfeasible to align the filters in an absolutely coplanar manner in the filter wheel, we include certain tilt angles of the optical filters with respect to the optical axis into our model.

We distinguish between two different kinds of aberrations, the *longitudinal* and *transversal* aberrations. Longitudinal aberrations are generated when the rays originating from one object point coincide behind or in front of the sensor plane instead of on the sensor plane itself and, thus, produce a blurred image. They can be interpreted as a *focusing* problem. In the context of multispectral imaging, this kind of aberrations is discussed in [14] and [16]. Transversal aberrations describe a wavelength-dependent projection of object points onto the sensor plane. For example, an object point with a white electromagnetic spectrum is not projected to exactly one position on the sensor plane; in fact, shorter wavelengths are projected to a different position than longer wavelengths. With respect to the optical bandpass filters, we already discussed these aberrations in [17], [18].

Different sources generate the previously mentioned types of aberrations. Like in an RGB camera, *chromatic* aberrations are caused by the wavelength-dependency of the properties of the lens. Although there are lenses compensating these distortions, a small wavelength-dependency remains. In our filter wheel camera, additional aberrations are caused by the optical filters, which all exhibit different thicknesses, refraction indices and are slightly tilted due to mechanical imperfections. When the passband images acquired with the different bandpass filters are then combined to an RGB image without compensation, color fringes as shown in Fig. 6(a) appear.

In our earlier work [17], [18], we chose a spectral reference passband and geometrically transformed the other passband images to match the reference passband. In other words, the reference passband was taken as the geometric reference. All passbands are, thus, aligned to the reference passband, i.e., the color fringes disappear, but the geometric distortions of the reference passband remain in all other passbands. As, due to lens imperfections, the reference passband exhibits lens distortions itself, a distortion-free imaging cannot be ensured. In this contribution, we use a calibration target as an absolute reference and also compensate the distortions in the reference passband. Unlike in our earlier work in [18], no registration algorithms are needed, since we utilize the checkerboard corner positions of the reference target.

Fig. 2 shows our basic concept: we treat each filter wheel position as a separate camera system which we calibrate individually. We describe the calibration model as well as the geometric model between the passbands.

Optical bandpass filters can be regarded as a plane-parallel plate (see Fig. 5). In the literature, we found contributions from Gao *et al.* [19], [20] and Shimizu *et al.* [21], who use a plane-parallel plate to acquire stereo images with a single camera. Although their aim is depth estimation, some of their considerations are relevant for our work as well. Other aspects deviate from our system: we utilize seven optical bandpass filters, whereas Gao and Shimizu use only one plate. Additionally, Gao places the plate in front of the camera, while our filter wheel is positioned between lens and sensor. In [22], a camera being shifted by two actuators is presented, which uses small movements of the camera to achieve a higher resolution. Alternatively, the insertion of a plane-parallel plate between lens and sensor is proposed to generate small image displacements. However, the paper does not provide a physical model and also does not account for lens or filter distortions.

In [18], we listed several papers describing the registration of passband images in a multispectral camera, e.g., [23]–[27]. We concluded that none of the mentioned papers provides a physical background of the distortions. Additionally, they do not account for distortions caused by the lens.

In the following section, we start with a description of the camera calibration model for each channel, develop a physical model and its approximation for a single bandpass filter, and then extend the model to describe the complete filter wheel. We then derive an algorithm for both the camera calibration and the final compensation of the image. In Section IV, we give detailed results, including a description of our system and calibration conditions, and provide reprojection errors and simulation results. Finally, we conclude the paper with a discussion.

Compared to an earlier conference version of this paper [28], we improved the model to make the calibration easier but yet accurate. We also provide a detailed description of the model with additional explanatory schematic diagrams. Besides a new bandpass filter simulation, we give more detailed results including several vector fields. Compared to our previous work in [18], we are not only able to compensate the color fringes, i.e., geometric misalignments between the spectral passbands. At the

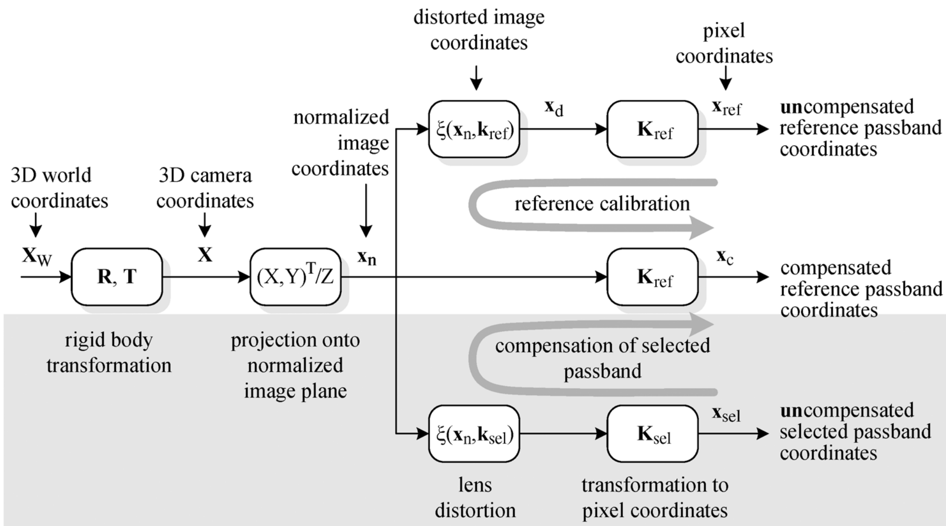

Fig. 4. Schematic diagram of our calibration. Horizontally arranged blocks subdivide different coordinate systems, vertically arranged blocks refer to different output images. The coordinates of the reference $()_{\mathrm{ref}}$ and a selected $()_{\mathrm{sel}}$ passband are separated by a gray background.

cost of using an additional calibration target and an alternative new calibration method, we are able to compensate lens distortions as well. We furthermore provide a more elegant derivation for the filter distortions.

II. Physical Model

A. Camera Calibration

We start with a description of our pinhole geometry camera model [29]–[31] shown in Fig. 3, which is complemented by a more schematic view including our terminology in Fig. 4. A 3-D point is defined by its 3-D world coordinates $\mathbf{X}_w \in \mathbb{R}^{3\times 1}$ or 3-D camera coordinates $\mathbf{X} = (X, Y, Z)^T$. The transformation between both coordinate systems is the rigid body transformation

$$\mathbf{X} = \mathbf{R}\mathbf{X}_w + \mathbf{T} \tag{1}$$

with rotation matrix $\mathbf{R} \in \mathbb{R}^{3\times 3}$ and translation vector $\mathbf{T} \in \mathbb{R}^{3\times 1}$. This step is shown in the first block in Fig. 4.

The 3-D camera point $\mathbf{X} = (X, Y, Z)^T$ is then projected onto a normalized image plane, which is positioned at $Z = 1$, to the normalized image point

$$\mathbf{x}_n = \begin{pmatrix} x_n \\ y_n \end{pmatrix} = \frac{1}{Z}\begin{pmatrix} X \\ Y \end{pmatrix}. \tag{2}$$

The image center of the normalized image points is given by the intersection of the optical axis-which is identical to the Z-axis of the camera coordinate system-with the sensor plane.

In [32] it is shown that lens distortions are radially symmetric relative to the image center. With respect to Fig. 3, this implies that all distortions depend upon the distance of the normalized image point $\mathbf{x}_n$ to the image center. The radius is given by

$$r_n^2 = x_n^2 + y_n^2. \tag{3}$$

According to [32, Eq. (20)] and [33, Eq. (4–5)], the distorted image coordinates $\mathbf{x}_d = (x_d, y_d)^T$ can then be computed

$$\begin{aligned}\mathbf{x}_d &= \left(1 + k_1 r_n^2 + k_2 r_n^4\right)\mathbf{x}_n + \begin{pmatrix} 2k_3 x_n y_n + k_4\left(r_n^2 + 2x_n^2\right) \\ k_3\left(r_n^2 + 2y_n^2\right) + 2k_4 x_n y_n \end{pmatrix} \\ &= \xi(\mathbf{x}_n, \mathbf{k}).\end{aligned} \tag{4}$$

Radial distortions are accounted for by the coefficients k_1, k_2 and are located on the connecting line between the image center and the normalized image point. Tangential distortions are orthogonal to the radial ones and are accounted for by the coefficients k_3, k_4. All distortions are described by the function $\xi()$, which takes a normalized, undistorted point $\mathbf{x}_n$ as input and a coefficient vector $\mathbf{k} = (k_1, k_2, k_3, k_4)^T$ as parameter.

The distortion operation is performed in normalized image coordinates to keep the influence of the actual focal length to a minimum. The distorted, normalized image coordinates $\mathbf{x}_d$ now have to be mapped to the actual pixel coordinates $\mathbf{x}$ by

$$\mathbf{x} = \mathbf{K}\begin{pmatrix} \mathbf{x}_d \\ 1 \end{pmatrix} \tag{5}$$

with the camera matrix

$$\mathbf{K} = \begin{pmatrix} f/s_x & 0 & c_x \\ 0 & f/s_y & c_y \end{pmatrix}. \tag{6}$$

The focal length of the lens is denoted by f, the size of the sensor pixels by s_x, s_y and the image center by $\mathbf{c} = (c_x, c_y)^T$. The *intrinsic* parameters of the camera are the camera matrix $\mathbf{K}$ and the distortion parameter vector $\mathbf{k}$.

B. Single Bandpass Filter Model

Up to now, the optical bandpass filters of the multispectral camera have not been considered yet. Fig. 5 shows a sketch of the imaging model including an optical filter: the filter with refraction index n_2 and thickness t is located between the projection center $\mathbf{0}$ and the sensor plane. Because it is practically not feasible to align the filters in an absolutely coplanar manner

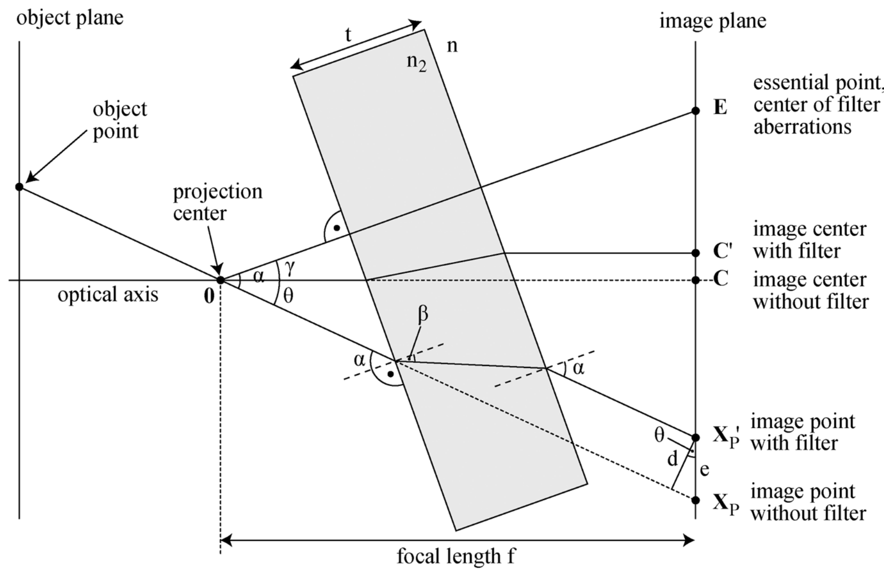

Fig. 5. Physical model of our multispectral camera. Points in the object plane are projected on the sensor plane throughout the optical filter. The filter with the thickness t and the refraction index n_2 is tilted by a small angle γ relative to the optical axis, and causes both object rays and the image center to be shifted.

with respect to the sensor, each filter is tilted by an individual small angle γ. Light rays which originate from object points are refracted when they enter the filter, then pass through the filter under a different angle, and leave the filter parallel but shifted with respect to the original ray. Therefore, the original image point $\mathbf{X}_P$, which lies on the intersection of the dashed line with the image plane, is shifted to a different position $\mathbf{X}'_P$. Also, rays lying on the optical axis which would normally hit the sensor in the *image center* $\mathbf{C}$, are shifted by the filter. In other words, the image center $\mathbf{C}$—which is identical to the distortion center in (4)—is shifted to $\mathbf{C}'$ when inserting an optical filter. The only rays which are not refracted are the ones hitting the filter perpendicularly.

We define several characteristic points in the image plane (see Fig. 5). The image center $\mathbf{C} = (0, 0, f)^T$ is the point where the optical axis $\mathbf{e}_z = (0, 0, 1)^T$ intersects with the sensor. Because of the refractions of the optical filter, the image center is shifted to $\mathbf{C}' \in \mathbb{R}^{3\times 1}$. A ray passing through the projection center $\mathbf{0} = (0, 0, 0)^T$ which hits the filter perpendicularly is not refracted and, thus, does not cause distortions in the image. We call the intersection of this specific ray with the image plane the *essential point* $\mathbf{E} = (E_x, E_y, f)^T$. Assuming small tilt angles of the filter (which is justified in practice), the image distortions are radially symmetric with respect to this point, in the same way as the image center is the center for lens distortions as shown previously. All undistorted image points $\mathbf{X}_P$ are distorted into the direction of the essential point $\mathbf{E}$ (see Fig. 10) because the optical refraction index of the filter is larger than that of the surrounding air and rays are, therefore, deflected towards the filter normal.

A ray passing through the projection center $\mathbf{0}$ and which, if not refracted, would hit the image plane at the image point $\mathbf{X}_P = (X_p, Y_p, f)^T$ (dashed line), impinges on the filter under an angle α relative to the filter normal. This angle occurs also between the segments $\overline{\mathbf{0E}}$ and $\overline{\mathbf{0X}_P}$, i.e., between the vector $\mathbf{E}$ and $\mathbf{X}_P$, and is given by

$$\cos\alpha = \frac{\mathbf{E}^T\mathbf{X}_P}{||\mathbf{E}||\,||\mathbf{X}_P||}. \tag{7}$$

The displacement d caused by the optical filter is then given [34, p. 101] by

$$d = t\sin\alpha\left(1 - \sqrt{\frac{1-\sin^2\alpha}{n_2^2 - \sin^2\alpha}}\right). \tag{8}$$

It can be seen that the displacement depends upon the filter thickness t, the refraction index n_2 and the incident angle α. Since α depends upon the filter tilt angle γ, the filter pose directly influences the displacement.

The relation between the parallel displacement d and the image plane displacement e is given by

$$\cos\theta = \frac{\mathbf{C}^T\mathbf{X}_P}{||\mathbf{C}||\,||\mathbf{X}_P||} = \frac{d}{e}. \tag{9}$$

The more the image point is away from the image center, the larger the difference between d and e becomes. With $\mathbf{C} = (0, 0, f)^T$ and $\mathbf{X}_P = (X_p, Y_p, f)^T$, (9) simplifies to

$$\cos\theta = \frac{f^2}{f||\mathbf{X}_P||} = \frac{f}{||\mathbf{X}_P||} = \frac{d}{e} \tag{10}$$

and we obtain

$$e = d\frac{||\mathbf{X}_P||}{f} \tag{11}$$

without explicitly computing the angle θ.[1] The distorted image point $\mathbf{X}'_P$ can then be computed by

$$\begin{aligned}\mathbf{X}'_P &= e\frac{\mathbf{E}-\mathbf{X}_P}{\|\mathbf{E}-\mathbf{X}_P\|}+\mathbf{X}_P\\ &= d\frac{\|\mathbf{X}_P\|}{f}\frac{\mathbf{E}-\mathbf{X}_P}{\|\mathbf{E}-\mathbf{X}_P\|}+\mathbf{X}_P.\end{aligned} \tag{12}$$

The normalized vector $(\mathbf{E}-\mathbf{X}_P)/\|\mathbf{E}-\mathbf{X}_P\|$ pointing from the image point $\mathbf{X}_P$ to the essential point $\mathbf{E}$ indicates the circular symmetry around the essential point.

Eqs. (7), (8), and (12) completely describe the displacement in the image plane caused by the *optical filter*. Based on these equations we have performed a simulation to generate the vector field shown in Fig. 10, which also illustrates the role of the essential point $\mathbf{E}$. Details about the simulation parameters can be found in the results; we have chosen the parameters to resemble our real multispectral camera. Without loss of generality, the image center $\mathbf{C}$ is here assumed to be exactly in the center of the sensor. The essential point $\mathbf{E}$ is located in the top right corner of the sensor.

Each vector in the figure represents a distortion from the original point $\mathbf{X}_P$ to its distorted counterpart $\mathbf{X}'_P$. The contour lines represent the real length of the vectors. The radial symmetry around the essential point can be clearly seen. The distortion in the essential point is zero, i.e., $\mathbf{X}'_P = \mathbf{X}_P$ for $\mathbf{X}_P = \mathbf{E}$. The image center $\mathbf{C}$ is also distorted because of the filter and is shifted to $\mathbf{C}'$.

C. Approximation of the Bandpass Filter Model

Practically for almost all multispectral cameras, each position in the filter wheel is indeed occupied by an optical filter. While this does not alter the validity of our model, it complicates or even prevents the estimation of some parameters described previously, because it is not possible to acquire a reference image which is not distorted by a filter. For example, the genuine image center $\mathbf{C}$ cannot be estimated from images acquired because it is always shifted to the filter-dependent displaced center $\mathbf{C}'$. The essential point $\mathbf{E}$ could be estimated by comparing images which have been taken with and without optical filter; image points without distortions would indicate the position of the essential point. However, since the reference image without optical filter cannot be acquired, it is not feasible to estimate the essential point $\mathbf{E}$.

We, therefore, approximate the exact model for the distortions caused by the filter. The results in this paper will show that the accuracy of such a model is sufficient: the mean errors are below one tenth of a pixel and are, thus, negligible.

For small angles, (8) simplifies [34, p. 102] to

$$d \approx t\left(1-\frac{1}{n_2}\right)\alpha \tag{13}$$

using the approximation $\sin\alpha \approx \alpha$ and $\sin^2\alpha \ll 1$. Furthermore, (12) is approximated by

$$\mathbf{X}'_P \approx \mathbf{X}_P + d\frac{\mathbf{E}-\mathbf{X}_P}{\|\mathbf{E}-\mathbf{X}_P\|} \tag{14}$$

by assuming that $\|\mathbf{X}_P\| \approx f$, i.e., the distance between the 3-D image point $\mathbf{X}_P$ from the optical axis is rather small compared to f. The angle α between the vectors $\mathbf{E}$ and $\mathbf{X}_P$ is approximated by

$$\alpha \approx \frac{\|\mathbf{E}-\mathbf{X}_P\|}{f} \tag{15}$$

by assuming that the arc length αf approximately equals the secant $\|\mathbf{E}-\mathbf{X}_P\|$ and that the radius of the virtual circle is f. By inserting (13) and (15) into (14), the final approximated displacement is given by

$$\mathbf{X}'_P \approx \mathbf{X}_P + t\left(1-\frac{1}{n_2}\right)\frac{\|\mathbf{E}-\mathbf{X}_P\|}{f}\frac{\mathbf{E}-\mathbf{X}_P}{\|\mathbf{E}-\mathbf{X}_P\|} \tag{16}$$

or

$$\mathbf{X}'_P \approx \mathbf{X}_P\left[1-\frac{t}{f}\left(1-\frac{1}{n_2}\right)\right] + \mathbf{E}\frac{t}{f}\left(1-\frac{1}{n_2}\right). \tag{17}$$

The terms in brackets are fixed terms, which depend upon the optical properties of the filters (n_2, t) and the system (f). Eq. (17) yields a linear relationship: the left summand is a position-dependent displacement, which directly depends upon the image position $\mathbf{X}_P$. The right summand provides a global displacement depending upon the essential point position $\mathbf{E}$. When the filter is coplanar with the sensor, i.e., $\mathbf{E} = \mathbf{C} = (0, 0, f)^T$, the right summand of (17) has no influence on the image and there is no global displacement. In other words, the left summand of (17) describes a zoom of the image and the right summand indicates a global shift of the image.

Therefore, the effects of the geometric filter distortions can be integrated into the camera matrix $\mathbf{K}$ in (6), which includes the image center and focal length. To take different camera matrices for different spectral channels into account, the schematic diagram in Fig. 4 exhibits two camera matrices ($\mathbf{K}_{\mathrm{ref}}$ and $\mathbf{K}_{\mathrm{sel}}$) corresponding to two different passbands.

In our modeling, we used an extended pinhole model, which is a combination of a pinhole model and a lens distortion model, and is well-known in the computer vision. Real lenses, however, have a different path of rays. Since F-mount lenses have a distance from the lens flange to the focal plane of 46.5 mm, the focal length of a wide angle lens with 10 mm can only be attained by the use of a special optical lens group, which increases the back focal length (distance from last lens to image sensor). Therefore, the rays hit the sensor in a more perpendicular manner for the real lens, and the angles α between the filter normal and the rays are decreased. This makes our previous approximations, which are based upon the assumption of small angles, even more accurate. To account for the different focal lengths, we substitute the focal length f in (17) with the back focal length f_{bfl}. It is not required that the focal lengths in (17) and (6) are equal since the former equation with the back focal length only induces a slight change of the focal length in the lens model.

D. Filter Wheel Model

Table I gives an overview of the variables discussed in the previous sections which characterize the camera. Most of the variables depend upon the spectral passband. Each passband uses a

[1]Note that, in 3-D, in general $\alpha \neq \gamma + \theta$.

TABLE I
VARIABLES CHARACTERIZING ONE PASSBAND OF OUR MULTISPECTRAL CAMERA; THE ASTERISKS MARK VARIABLES WHICH ARE FINALLY USED FOR COMPENSATION

c_x, c_y	*	camera center
f	*	focal length
$\mathbf{k}$	*	distortion coefficients
$\mathbf{R}$		rotation matrix
$\mathbf{T}$		translation vector
s_x, s_y		physical pixel size
$\mathbf{E}$		filter essential point
t		filter thickness
n_2		filter refraction index

different optical filter, which differs from the others in its properties like thickness, refraction index and essential point (or its tilt angle γ). Parameters such as focal length and image center, and correspondingly the camera matrix $\mathbf{K}$, therefore, differ from one spectral passband to the next. Thus, the dialing of the bandpass filter via the filter wheel can be regarded as an alteration of the optical system. The lens distortion coefficients also depend upon the wavelength because the optical properties of the lens glass are wavelength-dependent. Even though modern *apochromatic* lenses are constructed such as to compensate these dependencies, small *chromatic aberrations* remain.

The resulting complete model for both lens and filter distortions is shown in Fig. 4. Since the rotation matrix $\mathbf{R}$ and translation vector $\mathbf{T}$ are assumed not to be wavelength-dependent, the normalized image coordinates $\mathbf{x}_n$ are the same for all passbands. After that, the diagram path splits up into the reference passband and a selected passband. The "uncompensated reference passband coordinates" are given by the distortion function using the reference passband coefficients $\mathbf{k}_{\mathrm{ref}}$ (4) and the corresponding camera matrix $\mathbf{K}_{\mathrm{ref}}$. The second path in the middle of the figure depicts the compensated coordinates for the reference passband. The path shown in the shaded part of the figure represents the uncompensated coordinates of another passband we call the "selected" passband with its corresponding lens distortions coefficients $\mathbf{k}_{\mathrm{sel}}$ as well as the camera matrix $\mathbf{K}_{\mathrm{sel}}$. This is the passband compensated as described in the following to geometrically match the "compensated reference passband coordinates."

III. ALGORITHM

A. Camera Calibration for Lens Distortions

Camera calibration in this context is the estimation of the intrinsic and extrinsic camera parameters listed in the upper half of Table I, i.e., camera center, focal length, distortion coefficients, and so on. These parameters relate to the geometric distortions caused by the lens.

The parameters are estimated automatically from a set of calibration images of a checkerboard pattern shown in Fig. 9. Algorithms [29], [31], [35] performing the calibration usually take the subpixel-precise position of checkerboard crossings in the acquired images as input and then estimate the parameters. In our case, we use the well-known Bouguet toolbox [36] to realize the camera calibration (see also [37]), which provides both the checkerboard crossing extraction and final calibration. Since the parameters are different for each spectral passband, we run the calibration for each spectral passband. Because the extrinsic parameters like the rotation matrix $\mathbf{R}$ and the translation vector $\mathbf{T}$, which define the camera coordinate system with respect to the world coordinate system, are the same for all spectral passbands, we estimate these parameters only in the reference passband. For all other (selected) passbands, the extrinsic parameters are taken from the reference passband and we compute only the camera center, the focal length and the distortion parameter vector.

B. Rectification

After the camera parameters have been estimated as shown in the previous sections, the distortions have to be compensated. In the following, we focus without loss of generality on two spectral passbands—the *reference* and *selected* passband. The compensation of the other spectral passbands can be accomplished by choosing different *selected* passbands.

To ensure an equidistant sampling of the output image, we start with the undistorted coordinates of the final output image, i.e., with $\mathbf{x}_c = (x_c, y_c)^T$ and go back to the distorted coordinates of the input image $\mathbf{x}_{\mathrm{sel}} = (x_{\mathrm{sel}}, y_{\mathrm{sel}})^T$. In Fig. 4, we, thus, start at "compensated reference passband coordinates" on the right by evaluating each position in the reference image and go back to the "uncompensated selected passband coordinates" underneath. While the arrows in the figure indicate the theoretical signal path for the compensation, the practical signal path is the other way round because of the equidistant sampling. Using

$$\begin{pmatrix} \hat{u} \\ \hat{v} \end{pmatrix} = \mathbf{K}_{\mathrm{ref}}^{\mathrm{bwd}} \begin{pmatrix} x_c \\ y_c \\ 1 \end{pmatrix} \tag{18}$$

we first transform from pixel coordinates to normalized image coordinates with the backward camera matrix

$$\mathbf{K}_{\mathrm{ref}}^{\mathrm{bwd}} = \begin{pmatrix} s_x/f & 0 & c_x s_x/f \\ 0 & s_y/f & c_y s_y/f \end{pmatrix}. \tag{19}$$

In the diagram, we enter now the lower shaded part. We use

$$\begin{pmatrix} \tilde{u} \\ \tilde{v} \end{pmatrix} = \xi\left(\begin{pmatrix} \hat{u} \\ \hat{v} \end{pmatrix}, \mathbf{k}_{\mathrm{sel}}\right) \tag{20}$$

to apply the distortions caused by the *lens* in the selected passband. The function $\xi()$ provided in (4) computes the distortions using the distortion vector $\mathbf{k}_{\mathrm{sel}}$. The coordinates in the distorted selected passband corresponding to the "original" coordinates started out from in the compensated reference passband are then computed by

$$\begin{pmatrix} \hat{\mathbf{x}}_{\mathrm{sel}} \\ 1 \end{pmatrix} = \mathbf{K}_{\mathrm{sel}} \begin{pmatrix} \tilde{u} \\ \tilde{v} \\ 1 \end{pmatrix} \tag{21}$$

where $\mathbf{K}_{\mathrm{sel}}$ is the camera matrix for the selected passband.

The final compensation algorithm for a passband image with the wavelength λ_{sel} is now as follows: for each position $\mathbf{x}_c$ in the compensated destination image, the source position $\hat{\mathbf{x}}_{\mathrm{sel}}$ in the uncompensated selected passband image is computed using the equations in this section. The pixel value is taken from the source image using bilinear interpolation and transferred to the final image. This procedure is repeated for all image pixels and passbands. The results of this step are compensated passband images, which are geometrically aligned (registered) and do not exhibit lens distortions, e.g., pincushion or barrel distortions.

IV. Results

A. System Description and Calibration Conditions

We use a seven-channel multispectral camera (see sketch in Fig. 2) with a Sigma 10–20 mm F4–5.6 wide angle lens. Wide angle lenses tend to produce more distortions than normal lenses. The internal grayscale camera is a Sony XCD-SX900 with a chip size of 6.4 mm $\times$ 4.8 mm, a resolution of 1280 $\times$ 960 pixel and a pixel pitch of $4.65\ \mu\mathrm{m} \times 4.65\ \mu\mathrm{m}$. We use a C-mount camera, whereas the lens is a typical Nikon F-mount lens originally designed for 36 mm $\times$ 24 mm slides. Because the actual sensor size is smaller than the size of a slide, the focal length has to be multiplied by the *crop factor* 5.82. This factor is computed by dividing the sensor diagonal by the diagonal of the slide. The lens has an equivalent focal length range from 58.15 mm to 116.31 mm. The optical filters in our camera span a wavelength range from 400 nm to 700 nm with a bandwidth of 40 nm each and a wavelength distance of 50 nm.

We perform the camera calibration with the checkerboard pattern shown in Fig. 9, which features 9 $\times$ 7 squares with a unit length of 30 mm. Since we take only the crossings, all in all $8 \times 6 = 48$ points are used for calibration. We positioned the calibration target in 20 different poses and acquired a full multispectral image for each pose. Since one multispectral image consists in our case of seven grayscale images, this results in 140 images in total. For camera calibration, we use the Bouguet toolbox [36] and estimate a calibration parameter set for each spectral passband.

B. RGB Image Results

To visualize the multispectral images in the common sRGB color space, the passband images have been transformed using the methods in [38]. Each pixel is considered as a 7-D vector $\mathbf{v}_{\mathrm{cam}} \in \mathbb{R}^{7\times1}$; an interpolation matrix $\mathbf{M}_{7\to61} \in \mathbb{R}^{61\times7}$ produces a 61-D vector, which represents the quasi-continuous electromagnetic spectrum sensed by the pixel. Two other matrices transform from this spectrum to the XYZ color space ($\mathbf{M}_{\mathrm{XYZ}} \in \mathbb{R}^{3\times3}$) and finally to the sRGB color space ($\mathbf{M}_{\mathrm{sRGB}} \in \mathbb{R}^{3\times3}$). These operations can be combined into a single linear matrix operation

$$\mathbf{v}_{\mathrm{sRGB,lin}} = \mathbf{M}_{\mathrm{sRGB}}\mathbf{M}_{\mathrm{XYZ}}\mathrm{M}_{7\to61}\mathbf{v}_{\mathrm{cam}} \quad (22)$$

with $\mathbf{v}_{\mathrm{sRGB,lin}} \in \mathbb{R}^{3\times1}$. The final sRGB vector is then given by

$$\mathbf{v}_{\mathrm{sRGB}} = \mathbf{v}_{\mathrm{sRGB,lin}}{}^{1/2.2} \quad (23)$$

where 2.2 is an approximate gamma value defined by the sRGB color space, and where the exponentiation is done element-wise.

Some results of the color conversion are presented in Fig. 6, where crops from an X-Rite ColorChecker SG, a color test chart, are shown. Without any compensation, large color fringes are apparent in the image [Fig. 6(a)]. With the compensation algorithm presented in this paper, the color fringes vanish completely as shown in Fig. 6(b).

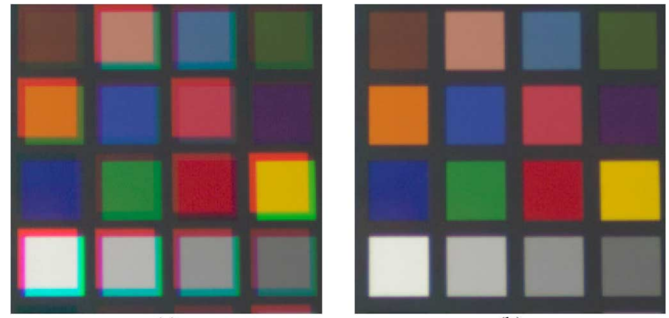

(a) (b)

Fig. 6. 200 $\times$ 200 pixel crops of images of the ColorChecker SG (a) without compensation and (b) with the described algorithm.

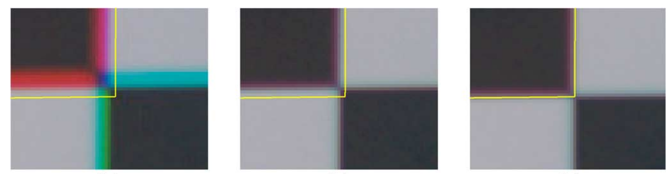

(a) (b) (c)

Fig. 7. 64 $\times$ 52 pixel crops of the detail area marked red in Fig. 8: (a) without geometric calibration, color fringes are clearly visible. (b) With the algorithm in [18], the color fringes are removed, but lens distortions remain. (c) Our present calibration scheme removes both color fringes and lens distortions.

Fig. 7 shows zoomed crops of one of our calibration images (see Fig. 8). The thin lines correspond to the edges of a distortion-compensated image like the one in Fig. 7(c). When the unaligned spectral passband images are combined to an RGB image as shown previously without any geometric calibration, large color fringes shown in Fig. 7(a) appear. With the algorithm presented in [18] (which does not require a calibration target), the color fringes vanish [see Fig. 7(b)], but the geometric distortions remain. The image edges are not aligned with the thin reference lines. While this might be sufficient for some applications, precise geometric measurements require distortion free images. Fig. 7(c) shows a crop of the compensated image, which has been computed using the algorithms in this paper. Both color fringes and geometric distortions are removed.

C. Measured Reprojection Errors

Fig. 8 shows a typical calibration image in the 550 nm passband. Thin yellow lines in the checkerboard pattern indicate the measured checkerboard crossings in the image. The (scaled) arrows point from these coordinates to the corresponding checkerboard positions in the 500 nm passband. Contour lines represent the length of the vectors, the largest vector on the checkerboard is approximately 1.75 pixels. The larger the vectors are, the worse the color fringes in Fig. 7(a) get. In terms of the schematic diagram in Fig. 4, the arrows point from *uncompensated reference passband coordinates* $\mathbf{x}_{\mathrm{ref}}$ to *uncompensated selected passband coordinates* $\mathbf{x}_{\mathrm{sel}}$.

The second column of Table II ("no calib.") gives the mean and maximum reprojection errors for all spectral passbands and all 20 calibration pattern poses. The displacements given here relate to the width of the color fringes in Fig. 7(a). The 550 nm passband is always taken as the reference passband, while the

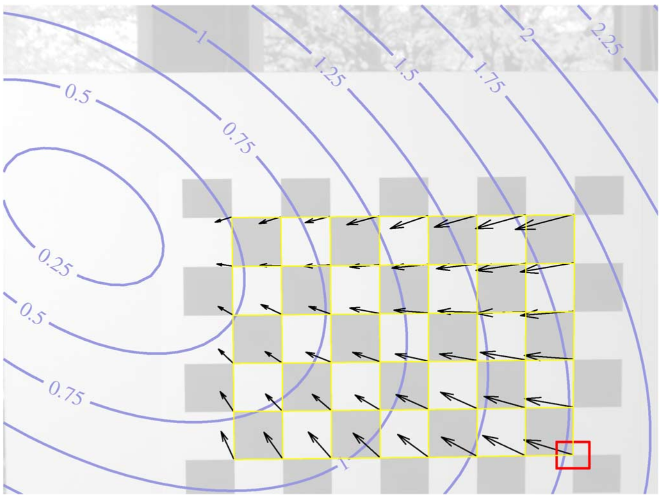

Fig. 8. Distortions caused by the bandpass filters; one of the 20 calibration pattern poses (no. 1) for passband 550 nm (reference passband); *scaled* arrows indicate distortions between this passband and the 500 nm passband selected. The contour lines show the real pixel displacement. A detail view of the area in the red rectangle is shown in Fig. 7.

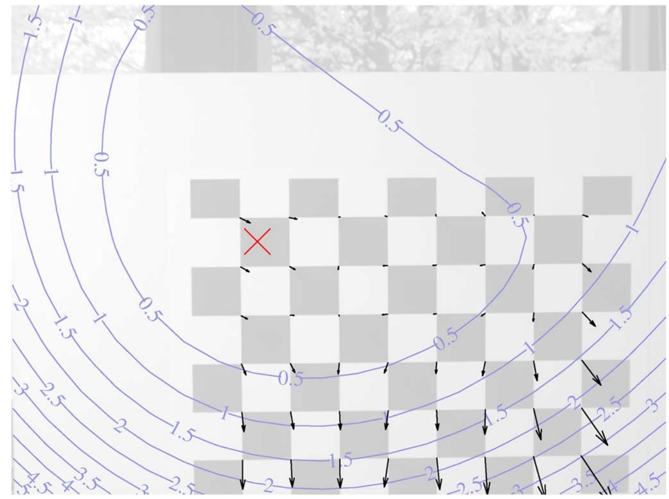

Fig. 9. Intra-band distortions in the 550 nm passband caused by the lens; (scaled) arrows point from distorted to undistorted pixel coordinates; the contour lines indicate the displacements in pixel; the distortion center $\mathbf{c}$ is marked with an "x." (Note that because of the tangential distortions the contour lines are not radially symmetric around the image center—although the distortions itself are radially symmetric.)

TABLE II
REPROJECTION ERRORS IN PIXELS FOR ALL SPECTRAL PASSBANDS. EACH ENTRY SHOWS THE MEAN OF EUCLIDEAN LENGTH AND MAXIMUM PIXEL ERROR, SEPARATED WITH A SLASH. FOR A DETAILED EXPLANATION SEE TEXT

	no calib.	intra-band	inter-band
400 nm	2.00 / 4.93	0.15 / 0.97	0.07 / 0.29
450 nm	1.24 / 2.60	0.14 / 0.95	0.05 / 0.23
500 nm	0.57 / 2.16	0.20 / 1.54	0.11 / 0.74
550 nm	0.00 / 0.00	0.14 / 0.96	0.00 / 0.00
600 nm	4.96 / 5.44	0.17 / 1.03	0.09 / 0.44
650 nm	2.17 / 3.29	0.15 / 0.98	0.05 / 0.27
700 nm	3.80 / 6.97	0.17 / 1.04	0.09 / 0.55
all	2.11 / 6.97	0.16 / 1.54	0.07 / 0.74

selected passband is indicated in the first column. For example, the maximum displacement between corresponding checkerboard crossings between the 500 nm and 550 nm spectral passband is 2.16 pixels. Thus, the maximum width of a color fringe as shown in Fig. 7(a) is 2.16 pixels, which is rather large. For the 550 nm row, both mean and maximum error vanish, since selected and reference passband are identical here.

Fig. 9 shows distortions in the 550 nm band, which are caused by the *lens* solely. In terms of the schematic diagram in Fig. 4, we measure the displacement between $\mathbf{x}_{n,\mathrm{ref}}$ and $\mathbf{x}_{d,\mathrm{ref}}$, namely the *normalized image coordinates* and the *distorted normalized image coordinates*, respectively. In our model, the distortions are caused by the lens distortion, which is described in (4) and exhibits a radial symmetry.

The column three ("intra-band") in Table II specifies the mean and maximum errors which are caused by the approximated lens model—they relate to the difference between the measured coordinates and the coordinates, which have been estimated using the lens model in (4). The column shows how well lens distortions can be compensated using this model. The errors denoted here relate to only one passband—the one given in the first column—and have no relation to other passbands. The column is, thus, entitled "intra-band." The mean errors are approximately one fifth of a pixel and, therefore, fully suffice for our calibration.

The last column in the table "inter-band" shows how well the coordinates of the reference passband and one of the selected passbands match after compensation. To measure this, the "uncompensated selected passband coordinates" $\mathbf{x}_{\mathrm{sel}}$ in Fig. 4 are transformed backwards to normalized image coordinates. After that, they are transformed forward to "estimated uncompensated reference passband coordinates" $\hat{\mathbf{x}}_{\mathrm{ref}}$ using (18) to (21) and compared to the measured coordinates $\mathbf{x}_{\mathrm{ref}}$. By doing so, the distortion models and camera matrices for both the reference and the selected passband are involved and the evaluation, therefore, incorporates the complete model. The error in the 550 nm row is zero since selected and reference passband coincide. The error of 0.11 in the 500 nm row means, that the estimated checkerboard crossing coordinates are on average 0.11 away from the true coordinates. The overall mean error of 0.07 shown in the last row is below one tenth of a pixel; in the compensated images, there will be no visible remaining artifacts.

D. Simulation Results

Fig. 10 shows our filter model simulation. We selected a filter thickness of $t = 5$ mm and a refraction index of $n_2 = 2.05$. As already mentioned in Section II-C, a real lens has a different path of rays than a pinhole model. To be more realistic, we take the F-mount back focal length $f_{\mathrm{bfl}} = 46.5$ mm as the focal length for our simulation. The essential point is located at $\mathbf{E} = (2\ \mathrm{mm}, 2\ \mathrm{mm}, f_{\mathrm{bfl}})^T$ on the sensor. We simulated only the usable part of the sensor with the size 5.93 × 4.46 mm. The image center is here chosen to be exactly in the center of the sensor, i.e., $\mathbf{C} = (0, 0, f_{\mathrm{bfl}})^T$, which might not hold for real sensors but does not affect our simulation. The distorted image center is at $\mathbf{C}' = (-0.1101\ \mathrm{mm}, 0.044\ \mathrm{mm}, f_{\mathrm{bfl}})^T$. Each (scaled) vector represents the displacement between an undistorted and distorted point, the contour lines specify the true vector length

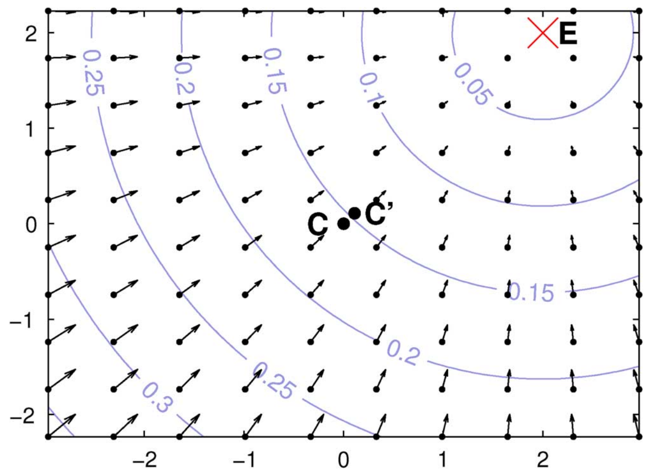

Fig. 10. Filter model simulation (excluding lens distortions) according to Fig. 5 and eq. (12) with the image center $\mathbf{C}$, the distorted image center $\mathbf{C}'$ and the essential point $\mathbf{E}$. Black dots represent original image positions $\mathbf{P}$, (scaled) arrows point into the direction of distorted points $\mathbf{P}'$. The contour lines indicate the real length of the vectors in millimeters. The radial symmetry around the essential point can be clearly seen.

in millimeters. A distortion of 0.2 mm corresponds to a pixel shift of approximately 43 pixels. The displacements given here are quite large because we examine the displacements between undistorted and distorted points, i.e., points without and with filter. In other words, the filter thickness is set to zero for the case without filter and to the actual thickness for the other case. In our multispectral camera system, the filter thickness variations are in the range of a few hundred micrometers.

We compared the exact simulation according to (12) to the approximation described in (17). The mean error is 0.065 pixel, the maximum error 0.33 pixel, which is by far sufficient for practical applications.

V. Conclusion

Compared to our earlier work in [18], where we were only able to compensate the distortions between different passbands, we are now able to compensate the lens distortions of the camera as well—at the cost of acquiring an additional calibration image. Therefore, the camera can not only be used for quantitative color image acquisition, i.e., measurement of the incident visible electromagnetic spectrum, but also for quantitative geometric measurements. Both color fringes and geometric distortions caused by the lens and the optical filters are compensated with our algorithm. Without calibration, the mean misalignment between the spectral passbands is 2.11 pixels, the maximum misalignment 6.97 pixels—these misalignments are clearly visible as color fringes in the transformed RGB image. By applying our algorithm, the mean calibration errors are reduced to 0.07 pixels, the maximum error to 0.74 pixels; the color fringes vanish completely and the image is geometrically corrected and may be used for measuring applications. Our calibration framework is based upon standard tools and the algorithm can be implemented easily.

In this contribution, the calibration requires a special calibration target and, therefore, allows for an absolute calibration compensating lens distortions. On the other hand, in [18], nearly all images are suitable for calibration, but lens distortions remain—though the color fringes are compensated as well.

Acknowledgment

The authors would like to thank Prof. B. Hill and Dr. S. Helling, RWTH Aachen University, for making the wide angle lens available.

References

[1] D. Steen and D. Dupont, "Defining a practical method of ascertaining textile color acceptability," *Color Research Appl.*, vol. 27, no. 6, pp. 391–398, 2002.

[2] S. Yamamoto, N. Tsumura, T. Nakaguchi, and Y. Miyake, "Development of a multi-spectral scanner using led array for digital color proof," *J. Imag. Sci. Technol.*, vol. 51, no. 1, pp. 61–69, 2007.

[3] V. Bochko, N. Tsumura, and Y. Miyake, "Spectral color imaging system for estimating spectral reflectance of paint," *J. Imag. Sci. Technol.*, vol. 51, no. 1, pp. 70–78, 2007.

[4] R. Luther, "Aus dem Gebiet der Farbreizmetrik," *Zeitschrift Tech. Phys.*, vol. 8, pp. 540–558, 1927.

[5] F. König and P. G. Herzog, "On the limitation of metameric imaging," in *Proc. Image Process., Image Qual., Image Capture, Syst. Conf.*, 1999, vol. 2, pp. 163–168.

[6] M. Yamaguchi, H. Haneishi, and N. Ohyama, "Beyond Red-Green-Blue (RGB): Spectrum-based color imaging technology," *J. Imag. Sci. Technol.*, vol. 52, no. 1, pp. 010 201-1–010 201-15, Jan. 2008.

[7] T. S. Hyvarinen, E. Herrala, and A. Dall'Ava, "Direct sight imaging spectrograph: A unique add-on component brings spectral imaging to industrial applications," *Proc. SPIE*, vol. 3302, pp. 165–175, May 1998.

[8] Cambridge Research & Instrumentation, Inc. [Online]. Available: http://www.cri-inc.com/

[9] R. Berns, L. Taplin, M. Nezamabadi, M. Mohammadi, and Y. Zhao, "Spectral imaging using a commercial color-filter array digital camera," in *Proc. 14th Triennal ICOM-CC Meeting*, The Hague, The Netherlands, Sep. 2005, pp. 743–750.

[10] H. Haneishi, S. Miyahara, and A. Yoshida, "Image acquisition technique for high dynamic range scenes using a multiband camera," *Color Research Appl.* vol. 31, no. 4, pp. 294–302, 2006.

[11] B. Hill and F. W. Vorhagen, "Multispectral image pick-up system," U.S. Patent 5,319,472, 1991, German Patent P 41 19 489.6.

[12] S. Tominaga, "Spectral imaging by a multi-channel camera," *J. Electron. Imag.*, vol. 8, no. 4, pp. 332–341, Oct. 1999.

[13] P. D. Burns and R. S. Berns, "Analysis multispectral image capture," in *Proc. Color Imag. Conf.*, Springfield, VA, 1996, vol. 4, pp. 19–22.

[14] A. Mansouri, F. S. Marzani, J. Y. Hardeberg, and P. Gouton, "Optical calibration of a multispectral imaging system based on interference filters," *Opt. Eng.*, vol. 44, no. 2, pp. 027 004.1–027 004.12, Feb. 2005.

[15] H. Haneishi, T. Iwanami, T. Honma, N. Tsumura, and Y. Miyake, "Goniospectral imaging of three-dimensional objects," *J. Imag. Sci. Technol.*, vol. 45, no. 5, pp. 451–456, 2001.

[16] J. Brauers and T. Aach, "Longitudinal aberrations caused by optical filters and their compensation in multispectral imaging," in *Proc. IEEE Int. Conf. Image Process.*, San Diego, CA, Oct. 2008, pp. 525–528.

[17] J. Brauers, N. Schulte, and T. Aach, "Modeling and compensation of geometric distortions of multispectral cameras with optical bandpass filter wheels," in *Proc. 15th Eur. Signal Process. Conf.*, Poznań, Poland, Sep. 2007, vol. 15, pp. 1902–1906.

[18] J. Brauers, N. Schulte, and T. Aach, "Multispectral filter-wheel cameras: Geometric distortion model and compensation algorithms," *IEEE Trans. Image Process.*, vol. 17, no. 12, pp. 2368–2380, Dec. 2008.

[19] C. Gao and N. Ahuja, "Single camera stereo using planar parallel plate," in *Proc. 17th Int. Conf. Pattern Recognit.*, N. Ahuja, Ed., 2004, vol. 4, pp. 108–111.

[20] C. Gao and N. Ahuja, "A refractive camera for acquiring stereo and super-resolution images," in *Proc. IEEE Comput. Soc. Conf. Comput. Vis. Pattern Recognit.*, N. Ahuja, Ed., New York, 2006, vol. 2, pp. 2316–2323.

[21] M. Shimizu and M. Okutomi, "Reflection stereo—Novel monocular stereo using a transparent plate—," in *Proc. 3rd Can. Conf. Comput. Robot Vis.*, M. Okutomi, Ed., Quebec City, Quebec, Canada, Jun. 2006, pp. 14–14.

[22] M. Ben-Ezra, M. Ben-Ezra, A. Zomet, and S. Nayar, “Jitter camera: High resolution video from a low resolution detector,” in *Proc. IEEE Comput. Soc. Conf. Comput. Vis. Pattern Recognit.*, A. Zomet, Ed., 2004, vol. 2, pp. 135–142.

[23] S. Helling, E. Seidel, and W. Biehlig, “Algorithms for spectral color stimulus reconstruction with a seven-channel multispectral camera,” in *Proc. 2nd Eur. Conf. Color Graph. Imag. Vis.*, Aachen, Germany, Apr. 2004, vol. 2, pp. 254–258.

[24] V. Cappellini, A. Del Mastio, A. De Rosa, A. Piva, A. Pelagotti, and H. El Yamani, “An automatic registration algorithm for cultural heritage images,” in *Proc. IEEE Int. Conf. Image Process.*, Genova, Italy, Sep. 2005, vol. 2, pp. 566–569.

[25] H. Foroosh, J. Zerubia, and M. Berthod, “Extension of phase correlation to subpixel registration,” *IEEE Trans. Image Process.*, vol. 11, no. 3, pp. 188–200, Mar. 2002.

[26] L. Lucchese, S. Leorin, and G. M. Cortelazzo, “Estimation of two-dimensional affine transformations through polar curve matching and its application to image mosaicking and remote-sensing data registration,” *IEEE Trans. Image Process.*, vol. 15, no. 10, pp. 3008–3019, Oct. 2006.

[27] G. Caner, A. M. Tekalp, G. Sharma, and W. Heinzelman, “Local image registration by adaptive filtering,” *IEEE Trans. Image Process.*, vol. 15, no. 10, pp. 3053–3065, Oct. 2006.

[28] J. Brauers and T. Aach, “Geometric multispectral camera calibration,” in *Proc. Scandinavian Conf. Image Anal.*, Oslo, Norway, Jun. 2009, pp. 119–127.

[29] R. I. Hartley and A. Zisserman*, Multiple View Geometry in Computer Vision*, 2nd ed. Cambridge, U.K.: Cambridge Univ. Press, 2004.

[30] R. Tsai, “A versatile camera calibration technique for high-accuracy 3D machine vision metrology using off-the-shelf TV cameras and lenses,” *IEEE J. Robot. Autom.*, vol. 3, no. 4, pp. 323–344, Aug. 1987.

[31] D. A. Forsyth and J. Ponce*, Computer Vision: A Modern Approach*. Upper Saddle River, NJ: Prentice Hall, Aug. 2002.

[32] D. C. Brown, “Close-range camera calibration,” *Photogram. Eng,*, vol. 37, no. 8, pp. 855–866, Jan. 1971.

[33] J. Heikkila and O. Silven, “A four-step camera calibration procedure with implicit image correction,” in *Proc. IEEE Comput. Soc. Conf. Comput. Vis. Pattern Recognit.*, Los Alamitos, CA, Jun. 1997, pp. 1106–1112.

[34] W. J. Smith*, Modern Optical Engineering*. New York: McGraw-Hill, 2000.

[35] Z. Zhang, “Flexible camera calibration by viewing a plane from unknown orientations,” in *Proc. Int. Conf. Comput. Vis.*, Corfu, Greece, Sep. 1999, vol. 7, pp. 666–673.

[36] J.-Y. Bouguet, Camera Calibration Toolbox for Matlab [Online]. Available: http://www.vision.caltech.edu/bouguetj/calib_doc/

[37] M. Mühlich and T. Aach, “High accuracy feature detection for camera calibration: A multi-steerable approach,” in *Proc. 29th Annu. Symp. German Assoc. Pattern Recognit.*, Heidelberg, Germany, Sep. 2007, pp. 284–292.

[38] J. Brauers, S. Helling, and T. Aach, “Multispectral image acquisition with flash light sources,” *J. Imag. Sci. Technol.*, vol. 53, no. 3, pp. 031 103-1–031 103-10, 2009.

Johannes Brauers received the diploma degree in electrical engineering from RWTH Aachen University, Germany, in 2005, where he is currently pursuing the Ph.D. degree.

His current research interests are multispectral imaging, in particular, modeling and compensation of geometric distortions, high dynamic range imaging, multispectral imaging with flash light sources, and the identification of the camera transfer function. He is an inventor for two patents.

Mr. Brauers received the “EADS Defence Electronics ARGUS Award 2005” for his M.S. thesis.

Til Aach (M’94–SM’02) received the diploma and doctoral degrees, both in electrical engineering, from RWTH Aachen University, Germany, in 1987 and 1993, respectively.

While working towards his doctoral degree, he was a Research Scientist with the Institute for Communications Engineering, RWTH Aachen University, in charge of several projects in image analysis, 3-D television, and medical image processing. From 1993 to 1998, he was with Philips Research Labs, Aachen, where he was responsible for several projects in medical imaging, image processing and analysis. In 1996, he was also an independent lecturer with the University of Magdeburg, Germany. In 1998, he was appointed a Full Professor and Director of the Institute for Signal Processing, University of Luebeck, Germany. In 2004, he became Chairman of the Institute of Imaging and Computer Vision, RWTH Aachen University. His research interests are in medical and industrial image processing, signal processing, pattern recognition, and computer vision. He has authored or coauthored over 230 papers. He is also a co-inventor of about 20 patents.

Dr. Aach has received several awards, including the award of the German “Informationstechnische Gesellschaft” (ITG/VDE), for a paper published in the IEEE Transactions on Image Processing in 1998. From 2002 to 2008, he was an Associate Editor of the IEEE Transactions on Image Processing. He was a Technical Program Co-Chair for the IEEE Southwest Symposium on Image Analysis and Interpretation (SSIAI) in 2000, 2002, 2004, and 2006, respectively. He is a member of the Bio-Imaging and Signal Processing Committee (BISP-TC) of the IEEE Signal Processing Society.